Article

Formation of Dense and High-Aspect-Ratio Iron Oxide Nanowires by Water Vapor-Assisted Thermal Oxidation and Their Cr(VI) Adsorption Properties

Faisal Budiman, Wai Kian Tan,* Go Kawamura, Hiroyuki Muto, Atsunori Matsuda, Khairunisak Abdul Razak, and Zainovia Lockman*
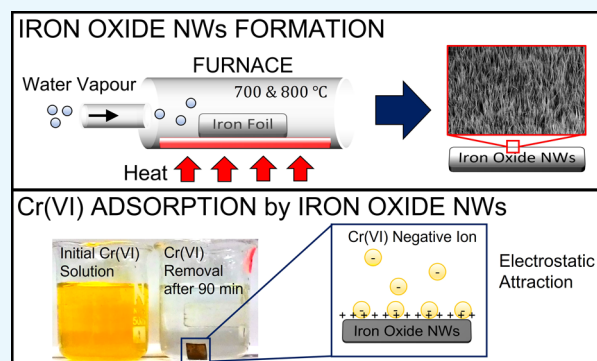
ACCESS | 📊 Metrics & More | 📖 Article Recommendations

ABSTRACT: Coral-like and nanowire (NW) iron oxide nanostructures were produced at 700 and 800 °C, respectively, through thermal oxidation of iron foils in air- and water vapor-assisted conditions. Water vapor-assisted thermal oxidation at 800 °C for 2 h resulted in the formation of highly crystalline α-Fe$_2$O$_3$ NWs with good foil surface coverage, and we propose that their formation was due to a stress-driven surface diffusion mechanism. The Cr(VI) adsorption property of an aqueous solution on α-Fe$_2$O$_3$ NWs was also evaluated after a contact time of 90 min. The NWs had a removal efficiency of 97% in a 225 mg/L Cr(VI) solution (pH 2, 25 °C). The kinetic characteristic of the adsorption was fitted to a pseudo-second-order kinetic model, and isothermal studies indicated that the α-Fe$_2$O$_3$ NWs exhibited an adsorption capacity of 66.26 mg/g. We also investigated and postulated a mechanism of the Cr(VI) adsorption in an aqueous solution of α-Fe$_2$O$_3$ NWs.

IRON OXIDE NWs FORMATION

FURNACE

Water Vapour | 700 & 800 °C

Iron Foil

Heat

Iron Oxide NWs

Cr(VI) ADSORPTION by IRON OXIDE NWs

Initial Cr(VI) Solution | Cr(VI) Removal after 90 min

Cr(VI) Negative Ion

Iron Oxide NWs

Electrostatic Attraction

1. INTRODUCTION

Chromium has oxidation states from (II) to (VI) but is the most stable in its trivalent (III) [Cr(III)] and hexavalent (VI) [Cr(VI)] forms; however, Cr(VI) rarely occurs naturally and originates from anthropogenic sources. Unlike Cr(III), Cr(VI) is toxic and carcinogenic.[1,2] Excessive inhalation of Cr(VI) can lead to lung cancer,[3] direct skin contact with it may result in dermatitis,[4] and when ingested, it can cause organ damage.[5] Cr(VI) compounds are, nonetheless, extremely important for electroplating, steel manufacturing, leather tanning, and textile production.[6] Inevitably, wastewater from these processes contains large amounts of Cr(VI), and unless properly treated, it can enter surface waters, causing harm to aquatic life and possibly entering the food chain. The World Health Organization has recommended that Cr(VI) concentrations in water should not exceed 0.05 mg/L;[7] therefore, total removal of Cr(VI) from industrial wastewater is crucial in order to prevent surface water concentrations exceeding this level.

There are several accepted methods for removing Cr(VI), which typically exists as highly soluble and toxic chromate anions (HCrO$_4^-$ or Cr$_2$O$_7^{2-}$), from industrial wastewater: photocatalytic reduction,[6,8−10] chemical precipitation,[11] electrokinetic remediation,[12] membrane filtration,[13,14] and adsorption.[15−17] Among these methods, adsorption is especially appealing, as it is very effective at removing Cr(VI).[18] The

adsorption process requires a solid surface (i.e., an adsorbent) with a large surface area for the species to be adsorbed (i.e., an adsorbate) to attach to, either by physical or chemical processes, for which in here, the use of a nanosized material will be beneficial for providing the surface area. Nanostructured materials can be defined as a material having an internal nanostructure or a surface nanostructure and present themselves as attractive large-surface-area adsorbents for this purpose, of which one-dimensional nanostructures, such as nanowires (NWs), are particularly effective.

Iron oxide is a compound material, largely found as hematite (α-Fe$_2$O$_3$), magnetite (Fe$_3$O$_4$), wüstite (Fe$_{1-x}$O), and maghemite (γ-Fe$_2$O$_3$),[19] which has attracted attention as an adsorbent due to its ability to remove various types of heavy-metal ions.[20−24] Recent studies have demonstrated that α-Fe$_2$O$_3$ has a high adsorption capability, which occurs through a chemisorption process involving the hydroxyl group on its surface.[25] Ren et al. investigated α-Fe$_2$O$_3$ in a fibrous form for

Cr(VI) ion removal and reported that the porous fiber-like morphology of α-Fe$_2$O$_3$ exhibited excellent adsorption of Cr(VI) from water, with rapid adsorption kinetics, high adsorption capacity, and good reusability.[26] In view of these results, we attempted to prepare α-Fe$_2$O$_3$ NWs through thermal oxidation of iron foils and investigated the sample's ability to remove Cr(VI) from aqueous solutions.

Thermal oxidation can be used to produce thin-film oxides composed of NWs.[27] Although there are various other ways of producing α-Fe$_2$O$_3$ NWs, such as electrospinning,[28,29] hydrothermal,[30] and nanocasting methods,[31] which produce NWs with a uniform diameter and length, they are known to be time-consuming, and post-annealing treatments are required for crystalline oxide formation. Thermal oxidation presents a simpler approach to forming surface oxide layers, and through careful control of the oxidation parameters, e.g., oxidation temperature,[32−35] unique nanostructures can be produced. Apart from temperature, the oxidation time and environment also affect the growth of NWs.[36] Our previous work explored the formation of iron oxide NWs by thermal oxidation in water vapor-assisted conditions.[33,35] The presence of water vapor during oxidation was found to induce more densely packed nanostructures with a uniform distribution compared with those under dry-air conditions; however, this work was performed at lower temperatures (400 −500 °C). Upon oxidation of iron at high temperatures, oxide scales consisting of multilayered oxides are formed. From the Fe−O phase diagram, oxidation of iron at either below or above 570 °C leads to the formation of different Fe oxide layers. Although our previous studies reported the formation of one- (1D) and two-dimensional iron oxide nanostructures, detailed investigations at higher temperature regimes (>570 °C) including the formation mechanism and Cr(VI) removal properties are not elucidated.

In this study, we investigated the formation of iron oxide nanostructures by thermal oxidation under water vapor-assisted conditions at high temperature regimes (i.e., 700 and 800 °C) and assessed the Cr(VI) removal capability of the samples. The growth of iron oxide NWs at these temperature regions under water vapor was systematically investigated, and the formation mechanism of high-aspect-ratio 1D Fe$_2$O$_3$ NWs and their Cr(VI) adsorption properties are reported. In regard to Cr(VI) adsorption behavior, the kinetic and equilibrium models were investigated, enabling the determination of the dynamic adsorptive property and the loading capacity of the formed Fe$_2$O$_3$ NWs. We found that the adsorptive behavior of the NW sample follows the Langmuir and pseudo-second-order kinetic models. Therefore, investigating these high-temperature oxidations further may result in novel and potentially useful nanostructures for various applications, including adsorption of toxic pollutants from contaminated water.

2. RESULTS AND DISCUSSION

2.1. Morphological Observations. FESEM images of the surface morphologies of the foils oxidized in dry air and water vapor at 700 and 800 °C are presented as Figure 1. It can be observed that different oxidation temperatures resulted in different morphologies, and it can be due to the dissimilarity of created stresses when the oxidation temperature is different. At 700 °C, the surface oxidization exhibited a coral-like structure, which was larger on the water vapor-oxidized sample than on the air-oxidized sample as shown in Figure 1a,b, respectively.
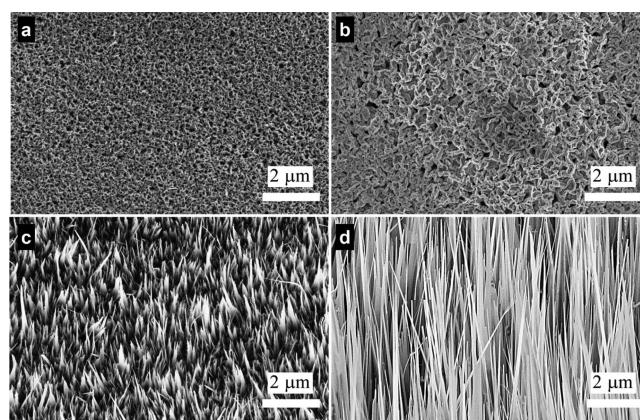

Figure 1. FESEM images of iron foils oxidized for 2 h in (a) 700 °C air, (b) 700 °C water vapor, (c) 800 °C air, and (d) 800 °C water vapor.

Micrographs of the foils oxidized at 800 °C in dry air and water vapor are presented in Figure 1c,d, respectively, and they show that the NWs formed on these foils were finer and longer (up to 20 μm) when oxidized in water vapor. This demonstrated that water vapor-assisted thermal oxidation strongly influenced the aspect ratio of the NWs.

To further investigate the effect of water vapor on the growth of the NWs, various oxidation durations were applied at 800 °C, and the resulting surface morphologies are illustrated in Figure 2. Interestingly, the NWs were formed after only 5 min of oxidation, as illustrated in Figure 2a, but the areal density was initially low with only sparse NWs formed on the foil surface. Here, areal density was defined as the number of NWs per measured area in an FESEM image. Extending the oxidation time to 15, 30, and 60 min increased the areal density of the NWs, as illustrated in Figure 2b−d, respectively, and oxidation for 120 min resulted in the formation of a dense, homogeneous NW surface, as illustrated in Figure 2e; therefore, we concluded that both the length and diameter of the NWs increased with increasing oxidation time. A summary of the morphological observations at 800 °C, including those of the length, aspect ratio, and areal density as a function of the oxidation time, is presented in Figure 3. These results indicate that controlled formation of α-Fe$_2$O$_3$ NWs can be achieved by controlling the oxidation time during water vapor-assisted thermal oxidation.

To gain an insight into the crystallinity of the NWs, we performed HR-TEM observations of a single α-Fe$_2$O$_3$ NW obtained through water vapor-assisted thermal oxidation at 800 °C for 2 h. The subsequent HR-TEM image is presented in Figure 4a, which indicates that the diameters of the bottom and tip of the nanowire were approximately 60 and 5 nm, respectively. The image also shows that the measured d-spacing was approximately 0.25 nm, which is in accordance with the (110) plane of α-Fe$_2$O$_3$. The tapered structure of the NWs was confirmed by the FESEM image in Figure 4b.

2.2. Crystal Phase of the α-Fe$_2$O$_3$ NWs. Figure 5a presents the XRD patterns of the iron foils oxidized at 800 °C for 2 h in air and water vapor. The XRD results indicated that the NWs consisted of crystalline structures with peaks indexed to hematite (α-Fe$_2$O$_3$) (ICDD no. 98-001-2733) and magnetite (Fe$_3$O$_4$) (ICDD no. 98-001-7319). It has been previously reported that following the thermal oxidation of iron, the outermost oxide layer is α-Fe$_2$O$_3$, and the underlying oxide is
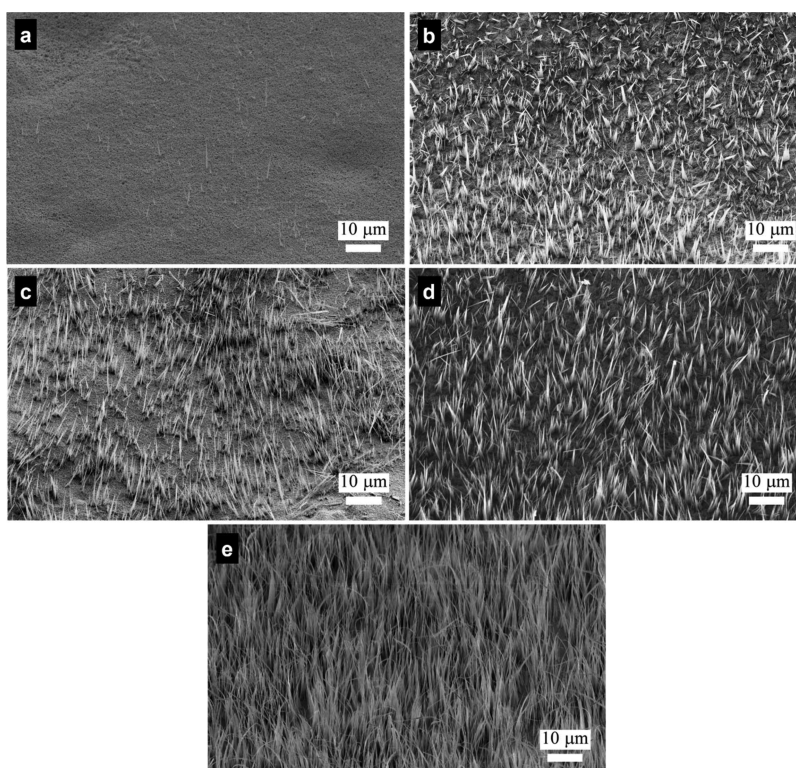
Figure 2. FESEM images of the oxidized iron at 800 °C in water vapor for (a) 5, (b) 15, (c) 30, (d) 60, and (e) 120 min.
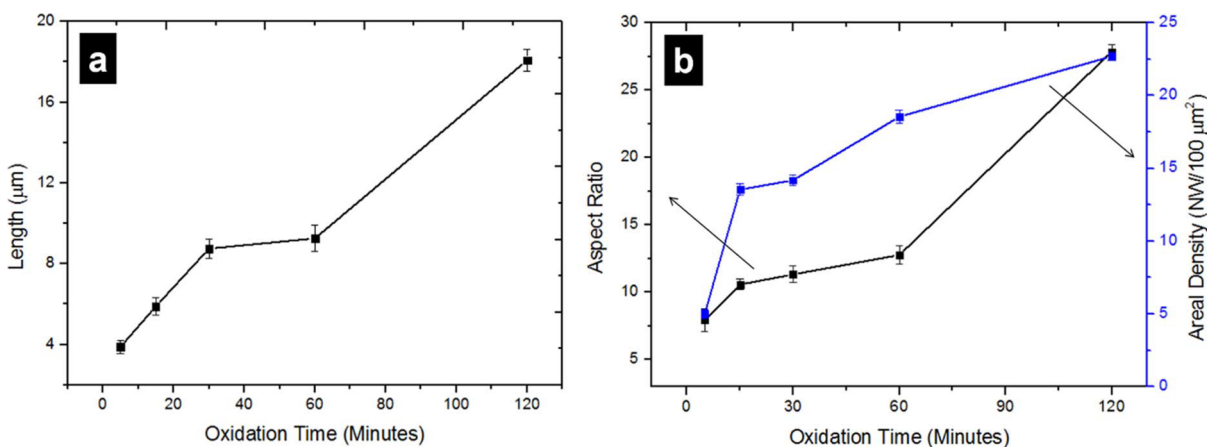

Figure 3. Quantitative analysis of (a) length, (b) aspect ratio, and areal density of the iron foils oxidized at 800 °C in water vapor for 5−120 min.
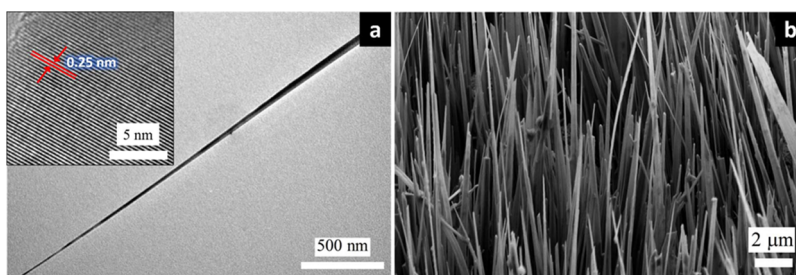

Figure 4. (a) HR-TEM image of a single α-Fe_2O_3 NW and (b) FESEM image of iron foil oxidized at 800 °C for 2 h in water vapor.

Fe_3O_4.[38] To verify this, we performed Raman spectroscopy. The Raman results are presented in Figure 5b and include bands at 227, 245, 293, 412, 499, and 612 cm^{-1}, which correspond to the α-Fe_2O_3 phase.[39] Owing to the low penetration depth of a Raman laser compared with XRD, we concluded that the outermost oxide layer was α-Fe_2O_3. Also, although the water vapor-assisted oxidation resulted in a
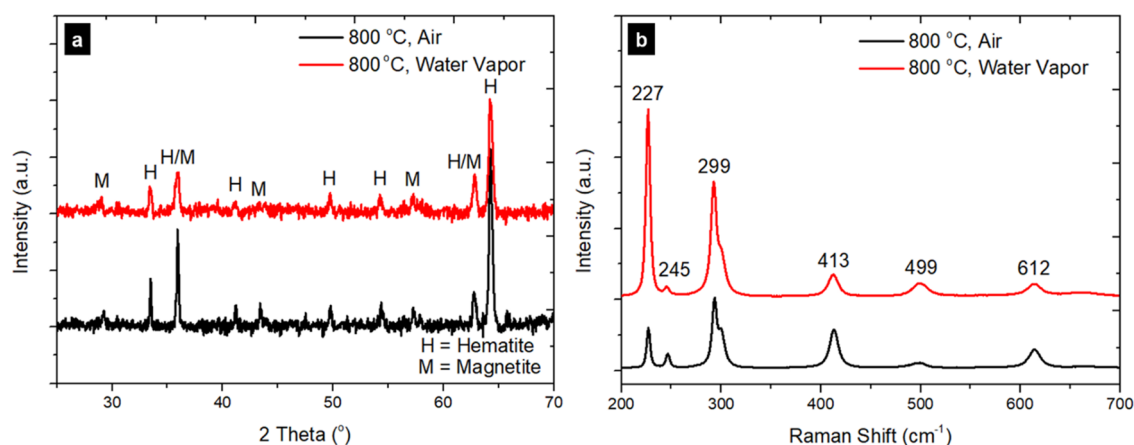
Figure 5. (a) XRD patterns and (b) Raman spectra of the iron foils oxidized at 800 °C for 2 h in air and water vapor.
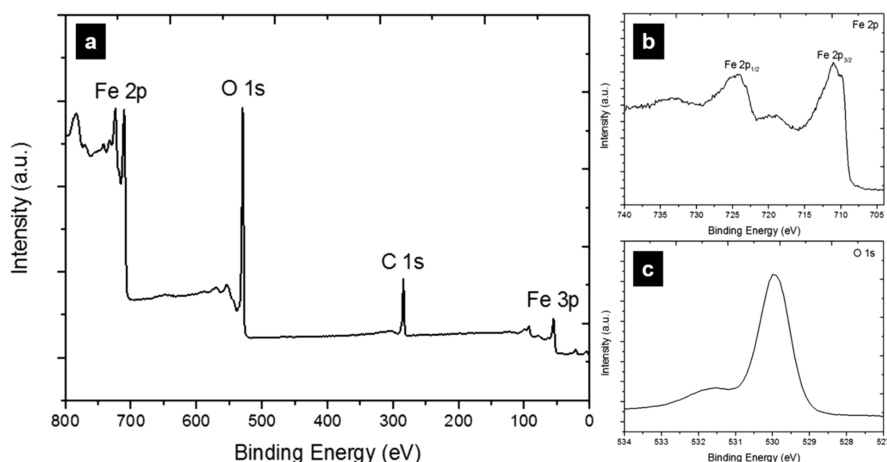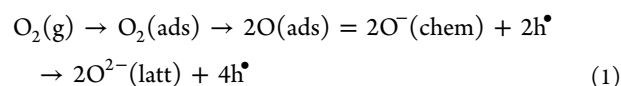

Figure 6. (a) Wide-scan, (b) Fe 2p, and (c) O 1s XPS spectra of iron foils oxidized at 800 °C in water vapor for 2 h.

denser formation of NWs, the outer α-Fe$_2$O$_3$ phase oxide layer was observed in the air-oxidized samples.

The surface elemental compositions of the foils oxidized at 800 °C for 2 h in water vapor were confirmed using XPS measurements. The obtained XPS spectrum is presented in Figure 6 and indicates the presence of Fe, O, and C in the α-Fe$_2$O$_3$ NWs, as shown in the wide-scan spectrum in Figure 6a. Figure 6b presents a high-resolution spectrum of Fe 2p, including two peaks at 724.4 and 709.9 eV, which correspond to Fe $2p_{1/2}$ and Fe $2p_{3/2}$, respectively. A binding energy difference of 14.5 eV and the absence of a peak at 719.0 eV suggested a predominant Fe^{3+} oxidation state, which further verified the presence of the α-Fe$_2$O$_3$ phase.[40] The O 1s peak, shown in Figure 6c, with a binding energy of 530 eV corresponds to the O^{2-} oxidation state in the oxide, and the second broad peak at 531.5 eV corresponds to the adsorbed oxygen or hydroxyl ions.[40] These XPS results further indicated that the outermost layer generated on the surface of the oxidized foils consisted of α-Fe$_2$O$_3$.

2.3. Growth Mechanism of the NWs. *2.3.1. Initial Oxidation Stage.* During dry-air thermal oxidation, the diffusion process is initiated by the chemisorption of oxygen onto the surface of the iron foil, forming a chemisorbed layer, which is then followed by the ionization of oxygen, forming O^{2-} (eq 1). The ionization of oxygen generates an electric field on the surface of the foil and triggers the oxidation of Fe (eq 2). Overall, the reciprocal diffusion of oxygen and iron

promotes the buildup of the oxide layer and forms a thin layer of iron oxide.

$$O_2(g) \rightarrow O_2(ads) \rightarrow 2O(ads) = 2O^-(chem) + 2h^\bullet$$
$$\rightarrow 2O^{2-}(latt) + 4h^\bullet \tag{1}$$

$$Fe \rightarrow Fe^{2+} + 2e^- \tag{2}$$

During water vapor-assisted thermal oxidation, the previously stable,[41] adsorbed water molecule dissociates as vapor (eqs 3 and 4).

$$H_2O(g) \rightarrow H_2O(ads) \tag{3}$$

$$H_2O \rightarrow H_2 + \frac{1}{2}O_2 \tag{4}$$

It has been reported that oxidation under water vapor conditions is accelerated compared with that in dry air, which may be due to the incorporation of a proton, accompanied by electrons, within the oxide scale during oxide growth. Fujii and Meussner reported that during oxidation in water vapor, the desorption of hydrogen from the oxide surface occurred (eq 5); this resulted in partial dissolution in the oxide[42] (eq 6). The small ionic radius of H atoms compared with those of Fe and O[43] means that H can interstitially bind with O as OH$_o$ in the oxide. The creation of such defects, compensated by electron deficiency, metal vacancies, and oxygen interstitials,

may in turn increase the oxidation rate, resulting in the increased rate of NW formation observed in this study.

$$2H_i^{\bullet} + 2e^- \rightarrow H_2 \tag{5}$$

$$H_2O(ads) \rightarrow OH_o{}' + H_i^{\bullet} \tag{6}$$

2.3.2. Formation of the Oxide Scale. The interaction of iron with reactive oxidative gases at high temperatures resulted in the formation of an oxide scale on the foil surface, as illustrated in the cross-sectional FESEM image in Figure 7.
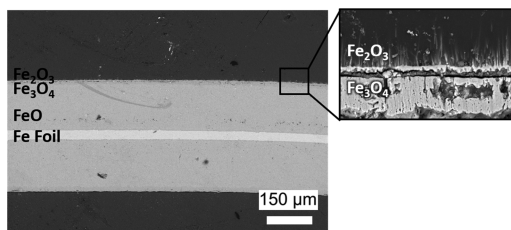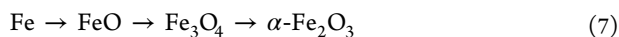

Figure 7. Cross-sectional FESEM image of iron foils oxidized at 800 °C in water vapor for 2 h.

This scale was composed of multiple layers of oxides, an outer layer of α-Fe$_2$O$_3$ and an inner layer of Fe$_{1-x}$O and Fe$_3$O$_4$, depending on the oxidization temperature. Fe$_{1-x}$O is thermodynamically unstable below 570 °C; thus, it was likely to be present during oxidation at the temperatures used in this study. The cross-sectional FESEM image in Figure 7 indicates that the Fe$_{1-x}$O layer was thicker than the Fe$_3$O$_4$ and α-Fe$_2$O$_3$ layers after oxidation at 800 °C for 2 h under water vapor-assisted conditions. Fe$_{1-x}$O is a nonstoichiometric compound with rich metal vacancies, which, through phase transformation, aids the growth of other phases during oxidation. Phase formation is thought to follow eq 7, with Fe$_{1-x}$O being transformed first to Fe$_3$O$_4$ and then to α-Fe$_2$O$_3$. The phase transformations during oxidation in dry air and water vapor are presented in Table 1.

$$Fe \rightarrow FeO \rightarrow Fe_3O_4 \rightarrow \alpha\text{-}Fe_2O_3 \tag{7}$$

2.3.3. Oxidation Growth Stress. The cross-sectional FESEM images in Figure 7 indicate that the surface region of the iron was composed of layered oxides in various phases, the presence of which generated stress within the oxide scale. During oxidation, thermal expansion leads to an increase in volume, which also contributes to oxide growth; however, this expansion resulted in a volume discrepancy of the iron and iron oxide, which induced a stress region at the metal–oxide interface. This caused the surface scale to be either in high compressive or tensile stress, especially at the interface regions; if the expansion of the outer oxide layer is larger than that of the oxide layer underneath, then a compressive stress develops (Pilling–Bedworth ratio > 1) in the upper oxide and a tensile stress develops in the underlying oxide. This discrepancy alters the diffusion rate of the growing species, leading to preferential growth of the oxide at the oxide–air interface in the *c*-axis direction.[38]

The relaxation of the generated stresses resulted in the growth of NWs at the surface by a mechanism illustrated in Figure 8. During the thermal oxidation process, Fe species diffuse and are accelerated across the oxide layer before nucleating on α-Fe$_2$O$_3$ grains through surface diffusion. This continuous and fast diffusion led to NW growth along the *c*-axis, which generated elongated oxide nanostructures, i.e., NWs. Observations under FESEM evidenced this phenomenon, with the nucleation and surface diffusion processes clearly seen in Figure 9a,b, respectively.

2.4. Evaluation of Cr(VI) Adsorption Using the α-Fe$_2$O$_3$ NWs. We then evaluated the Cr(VI) adsorption properties of the NWs using the α-Fe$_2$O$_3$ NWs obtained after thermal oxidation at 800 °C, both in air and water vapor. Pure iron foil was also assessed as a control sample. As shown in Figure 10a, the removal efficiency of Cr(VI) with an initial concentration at 200 mg/L was 13.5, 71, and 95% for pure iron and the samples oxidized in air and in water vapor atmospheres, respectively. These results indicate that the presence of water vapor promoted the formation of NWs with a larger surface area in comparison to those generated in air.

Moreover, further assessment of the samples obtained after water vapor-assisted thermal oxidation at 800 °C with various concentrations of Cr(VI) between 225 and 300 mg/L was conducted at room temperature. The results obtained are shown in Figure 10b, exhibiting a high Cr(VI) removal efficiency of >90% for each concentration. Here, we varied the concentration of the adsorbate according to the adsorption limit of the sample for evaluating the kinetic and equilibrium behavior. An equilibrium was reached after 90 min of contact between the NWs and the Cr(VI) solution. The adsorption profiles exhibited similar patterns across the various Cr(VI) solutions.

A unique amphoteric property of metal oxide offers the flexibility on shifting the surface charge of iron oxide, hence allowing either anion or cation adsorption from aqueous environments. The mechanism of those adsorptions is based on electrostatic attraction,[44] and it is pH-dependent.[14,45] The nature of Cr(VI) species is mostly found as a negative ion.[46] Such anion adsorption is preferred if performed in acidic

Table 1. Oxidation Reactions of Iron in Dry and Water Vapor-Assisted Conditions

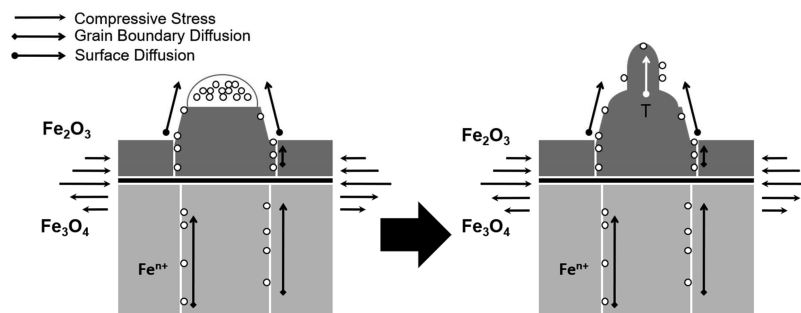|	Oxidation reaction in dry air	Oxidation reaction in water vapor
Air condition	$O_2 + 4e^- \rightarrow 2O^{2-}$	$H_2O \rightarrow OH_o{}^{\cdot} + H_i^{\bullet}$
Hematite (α-Fe$_2$O$_3$)	$2Fe^{3+} + 3O^{2-} \rightarrow Fe_2O_3$	$2Fe^{3+} + 3OH^- \rightarrow Fe_2O_3 + 3H^+$
Magnetite (Fe$_3$O$_4$)	$2Fe^{3+} + Fe^{2+} + 4O^{2-} \rightarrow Fe_3O_4$	$2Fe^{3+} + Fe^{2+} + 4OH^- \rightarrow Fe_3O_4 + 4H^+$
Wustite (Fe$_{1-x}$O)	$Fe^{2+} + O^{2-} \rightarrow FeO$	$Fe^{2+} + OH^- \rightarrow FeO + H^+$
Fe substrate	$Fe \rightarrow Fe^{2+} + 2e^-$	$Fe \rightarrow Fe^{2+} + 2e^-$

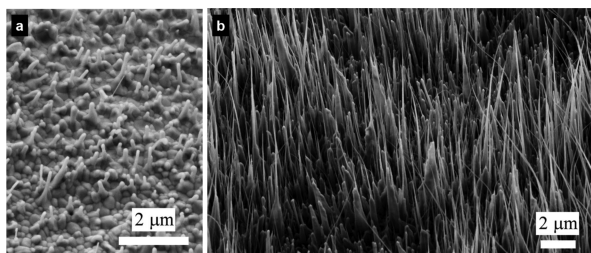**Figure 8.** Schematic illustration of the NW growth mechanism through thermal oxidation on an iron foil.


Figure 9. FESEM image showing (a) initial growth of NWs on α-Fe$_2$O$_3$ grains and (b) formation of NWs through surface diffusion.

conditions, as the adsorbent will be protonated due to the existence of H$^+$ ions. By considering that the lowest pH of the chromate ions as the HCrO$_4^-$ ion is at pH 2[46] and the point of zero charge (pH$_{zpc}$) of α-Fe$_2$O$_3$ has also been reported to be between pH 7.2 and pH 9.5,[47] the condition at pH 2 is reported to be the optimum pH for effective removal of Cr(VI).[48−54] Therefore, pH 2 was chosen for the Cr(VI) adsorption test in this study.

The mechanism of the Cr(VI) removal is described as follows: Upon the immersion of the Fe$_2$O$_3$ sample into Cr(VI) solution, hydroxylation of the surface (S) occurs generating an oxide surface that is covered with hydroxyl ions (OH$^-$), forming S−OH. In acidic Cr(VI) solution that is rich with H$^+$ ions, sorption of H$^+$ (protonation process) then leads to the formation of a positive surface charge at the iron oxide|solution interface as indicated in eq 8. The positively charged surface of Fe$_2$O$_3$ acts as an adsorbent to attract the negatively charged Cr(VI) species through electrostatic attraction, as shown in eq 9[55,56] and as illustrated in Figure 11a.

$$S - OH + H^+ \rightleftharpoons S - OH_2^+ \tag{8}$$

$$SOH_2^+ + HCrO_4^- \rightleftharpoons (SOH_2^+)HCrO_4^- + H_2O \tag{9}$$
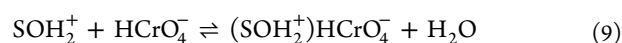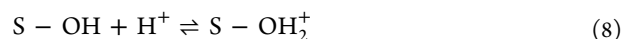
We also observed precipitates on the oxidized foil as shown in the inset of Figure 11b. There is a possibility that these precipitates are composed of Fe,Cr(OH)$_3$ as there is also a possibility of reduction occurring on the surface of the iron oxide. This is in accordance with Richard and Bourg whereby reduction of Cr(VI) is possible and the formation of Fe,Cr(OH)$_3$ precipitates can lead to the removal of Cr(III) completely.[57] In order to confirm the adsorption of Cr further, XPS was conducted. Figure 11b shows the spectra of Cr 2p with corresponding peaks on α-Fe$_2$O$_3$ NWs before and after the Cr(VI) adsorption process. The spectrum indicated the presence of Cr on the α-Fe$_2$O$_3$ NWs, at 585 and 575 eV after the adsorption process. The peaks correspond to the binding energies of Cr 2p$_{1/2}$ and Cr 2p$_{3/2}$, respectively.

Although the protonation of iron oxide is necessary for adsorption of the negatively charged Cr(VI) adsorption, this process also triggers Fe dissolution to occur.[15] The dissolution reaction is initiated by single-proton adsorption at a neutral surface OH/OH$_2$ pair, thus converting it into Fe(OH$_2$)$^{2+}$. Then, continuous adsorption of two protons at the same time would weaken the Fe−O bond, causing the dissolution of Fe from the oxide surface. However, this dissolution step is rate-limiting, as the activation energy is higher for dissolution to occur, compared to the protonation process.[15] Therefore in our case, the dissolved Fe ions further reacted with Cr(VI) species, reducing them to Cr(III) followed by precipitation. This indicates that there could be (minor) iron oxide
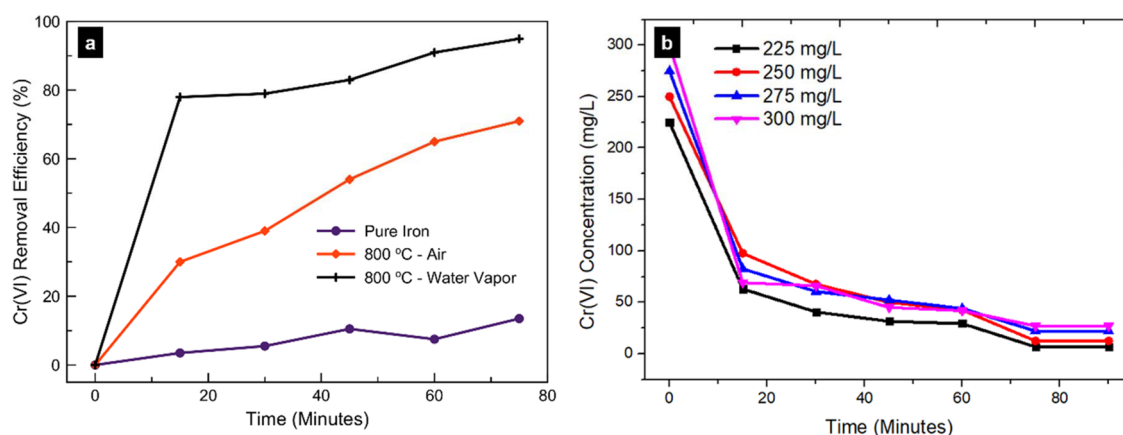

Figure 10. Cr(VI) adsorption profiles from Cr(VI) solution: (a) using the α-Fe$_2$O$_3$ NW samples synthesized at 800 °C in air and water vapor and (b) varying concentrations between 225 and 300 mg/L using α-Fe$_2$O$_3$ NWs obtained from thermal oxidation at 800 °C in water vapor.
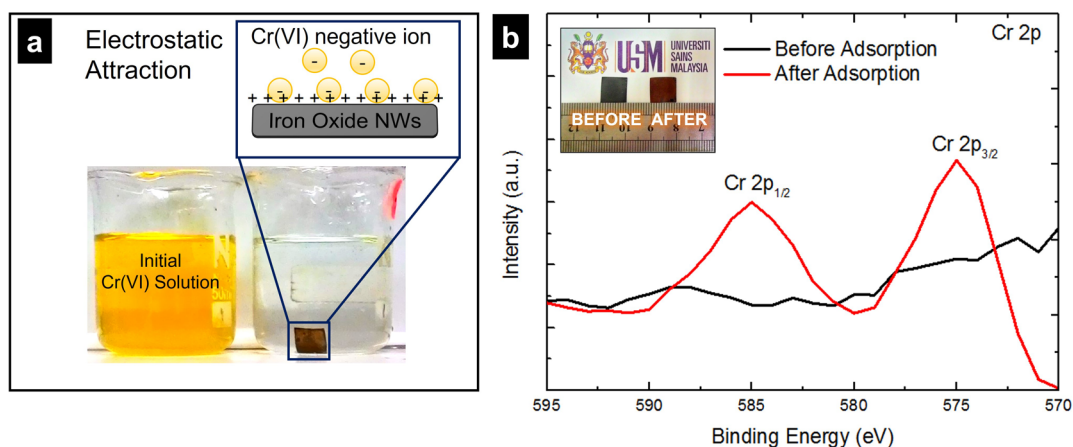
Figure 11. (a) Photograph showing the solution before and after the Cr(VI) adsorption process with an illustration of the surface adsorption mechanism (inset) and (b) XPS spectra of Cr 2p of the α-Fe$_2$O$_3$ NWs (before and after the Cr (VI) adsorption process).
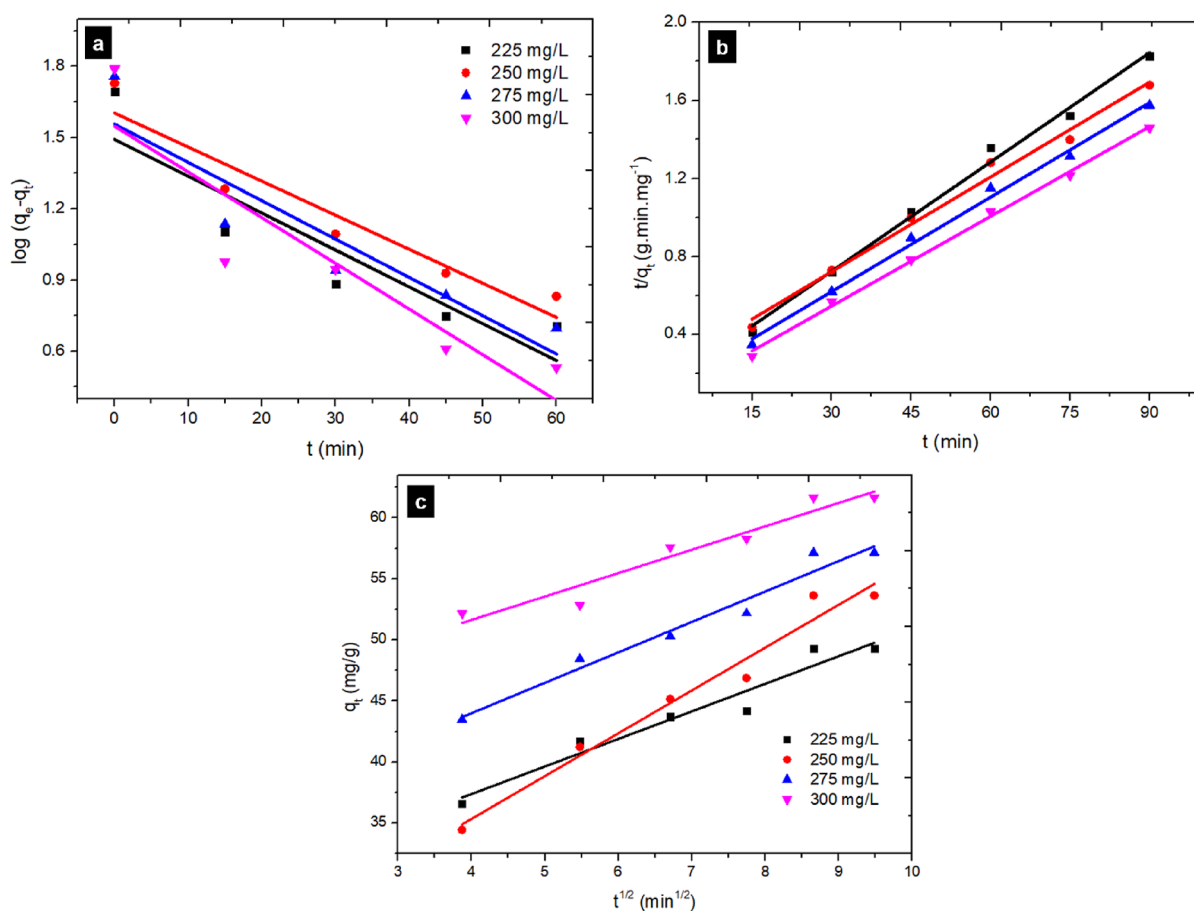

Figure 12. Linear fit of α-Fe$_2$O$_3$ NW kinetics to (a) pseudo-first-order kinetic, (b) pseudo-second-order kinetic, and (c) intraparticle diffusion models.

dissolution in acidic solution. Therefore, we deduce that our sample is more suitable to be used for single removal use. However, in terms of reproducibility, the Cr(VI) removal results shown in Figure 10b indicated a rather consistent removal property.

2.5. Determination of Adsorption Kinetics. Kinetic adsorption describes the rate of the adsorption process by monitoring the change of adsorbate concentration against time; thus, the dynamic movement of the adsorbate to the adsorbent can be predicted. By knowing the rate of adsorption,

we were able to investigate an appropriate kinetic model by fitting the data to several kinetic adsorption models: (1) pseudo-first-order, (2) pseudo-second-order, and (3) intraparticle diffusion, which are illustrated in Figure 12. The validity of the predicted models with the experimental data was determined using values of R^2, which are presented in Table 2 along with the corresponding correlation coefficients; the closer the value of R^2 to 1, the better the model fitted the adsorption kinetics of Cr(VI) in the tested system. The details of the fitting of each model are described below.

Table 2. Comparison of the Kinetic Models Fitted for Cr(VI) Adsorption

method	sample	R^2	kinetic rate constant
pseudo-first order	225 mg/L	0.77800	$k_1 = 0.03576$
	250 mg/L	0.88960	$k_1 = 0.03304$
	275 mg/L	0.80328	$k_1 = 0.03719$
	300 mg/L	0.78220	$k_1 = 0.00443$
pseudo-second order	225 mg/L	0.99159	$k_2 = 0.00214$
	250 mg/L	0.98664	$k_2 = 0.00111$
	275 mg/L	0.99300	$k_2 = 0.00194$
	300 mg/L	0.99692	$k_2 = 0.00027$
intraparticle diffusion	225 mg/L	0.93541	$k_{id} = 2.25689$
	250 mg/L	0.91151	$k_{id} = 3.50526$
	275 mg/L	0.92915	$k_{id} = 2.49014$
	300 mg/L	0.91090	$k_{id} = 1.91565$

2.5.1. Pseudo-First-Order Kinetic Model.

The linear fit of Cr(VI) adsorption on α-Fe$_2$O$_3$ NWs in accordance with a pseudo-first-order kinetic model is presented in Figure 12a. The pseudo-first-order model follows an adsorption process according to eq 10[58]

$$\frac{dq_t}{dt} = k(q_e - q_t) \tag{10}$$

By applying the initial condition, $q_t = 0$ at $t = 0$ and $q_t = q_t$ at $t = t$, the integration of the pseudo-first-order model can be expressed as eq 11

$$\log(q_e - q_t) = \log q_e - 0.434 k_1 t \tag{11}$$

where q_e and q_t are the total adsorbed Cr(VI) at equilibrium and at time t (mg g^{-1}), respectively, and k_1 is the pseudo-first-order kinetic constant (min^{-1}). The R^2 values for the pseudo-first-order kinetic model in Table 2 are below 0.8, indicating that the experimental data deviated from the theoretical data; therefore, this model was unsuitable.

2.5.2. Pseudo-Second-Order Kinetic Model.

The linear fit of Cr(VI) adsorption on α-Fe$_2$O$_3$ NWs according to the pseudo-second-order kinetic model is presented in Figure 12b. The pseudo-second-order kinetic model follows an adsorption process according to eq 12, which describes a kinetic rate driven by chemisorption[58]

$$\frac{dq_t}{dt} = k_2(q_e - q_t)^2 \tag{12}$$

By applying the initial condition, $q_t = 0$ at $t = 0$ and $q_t = q_t$ at $t = t$, the integration of the pseudo-second-order kinetic model can be expressed by eq 13

$$\frac{t}{q_t} = \frac{1}{k_2 q_e^2} + \frac{1}{q_e} t \tag{13}$$

where q_e and q_t are the total adsorbed chromium at equilibrium and at time t (mg g^{-1}), respectively. The value of k_2 is the rate constant of pseudo-second-order adsorption (g mg^{-1} min^{-1}). The R^2 values obtained for all the concentrations investigated were higher than 0.98 for the pseudo-second-order model, as shown in Table 2, indicating that it is appropriate to describe the dynamic behavior of Cr(VI) adsorption onto α-Fe$_2$O$_3$ NWs.

2.5.3. Intraparticle Diffusion Model.

The linear fit of Cr(VI) adsorption on α-Fe$_2$O$_3$ NWs according to the intraparticle diffusion model is presented in Figure 12c. The intraparticle diffusion model describes an adsorption process that occurs in multiple stages.[58] First, a sharp Cr(VI) concentration reduction indicates a spontaneous adsorption process. Second, a gradual adsorption is driven by a controlled diffusion phenomenon. Finally, the low concentration of the remaining adsorbate results in a slow adsorption process. The intraparticle diffusion model can be expressed using eq 14

$$q_t = k_{id}(t)^{1/2} + c \tag{14}$$

where q_t (mg g^{-1}) is the amount of Cr(VI) adsorbed, k_{id} is the rate factor (mg/g/min$^{1/2}$), and c (mg g^{-1}) represents the boundary layer thickness. The R^2 values for the intraparticle diffusion model, presented in Table 2, are close to 0.9, which are even lower than the values obtained for the pseudo-second-order kinetic model. This indicated that the intraparticle diffusion model was unsuitable.

2.6. Investigation on the Adsorption Equilibrium.

To determine the loading capacity of the adsorbent, we continued investigating the equilibrium. The adsorption data were fitted to the Langmuir and Freundlich models, and the obtained plots are presented in Figure 13. Similarly, in the kinetic study, the validity was determined by R^2 values, i.e., the closer the R^2
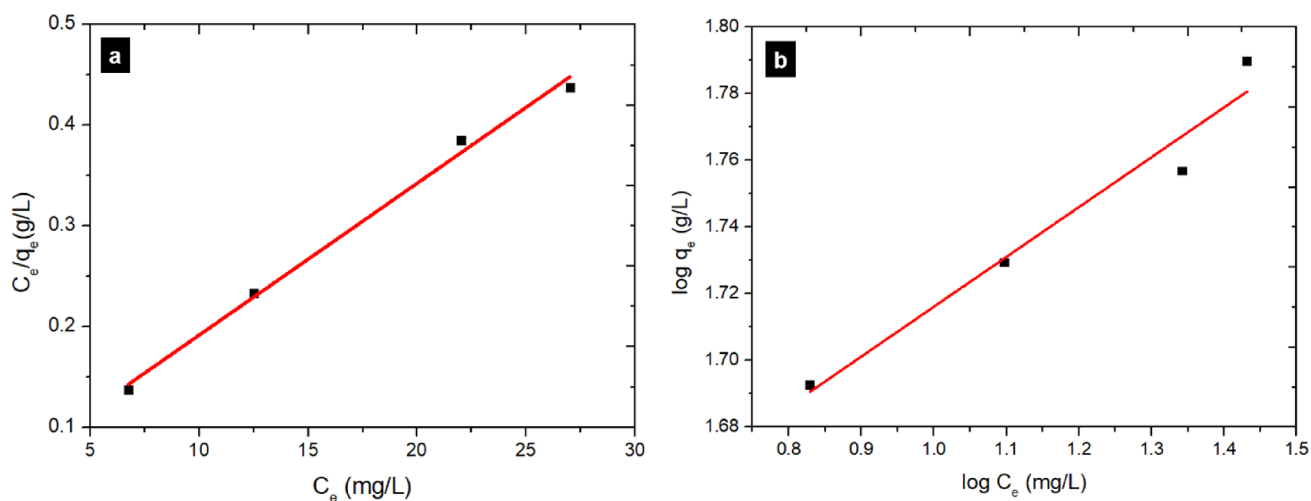
Figure 13. Linear fit of Cr(VI) adsorption equilibrium to (a) Langmuir and (b) Freundlich models.

was to 1, the better the fit of the model was. The correlation coefficient and the R^2 value for each model are presented in Table 3. Each model is described below.

Table 3. Summary of the Adsorption Equilibrium Modeling

Langmuir			Freundlich		
q_m (mg/g)	K_L	R^2	n	K_F	R^2
66.2690	0.37048	0.99209	6.68851	36.86888	0.94082

2.6.1. Langmuir Model. The linear fit of Cr(VI) adsorption on α-Fe$_2$O$_3$ NWs according to the Langmuir model is presented in Figure 13a. The Langmuir model describes an adsorption process that occurs across a homogeneous adsorbent surface,[59] which can be described by eq 15

$$\frac{C_e}{q_e} = \frac{1}{K_L \cdot q_m} + \frac{1}{q_m} \cdot C_e \tag{15}$$

where K_L (L mg^{-1}) is the Langmuir equilibrium constant and q_m (mg g^{-1}) is the monolayer capacity, which indicates the available active sites per mass of the sample where Cr(VI) could be adsorbed. The R^2 value for the Langmuir model was close to 0.99, indicating that it fitted the equilibrium behavior of Cr(VI) adsorption onto α-Fe$_2$O$_3$ NWs well. The calculated adsorption capacity of α-Fe$_2$O$_3$ NWs for Cr(VI) using the Langmuir model was approximately 66.2690 mg/g.

2.6.2. Freundlich Model. The linear fit of Cr(VI) adsorption on α-Fe$_2$O$_3$ NWs according to the Freundlich model is presented in Figure 13b. The Freundlich model describes an adsorption process that occurs across a heterogeneous adsorbent surface,[59] which can be described by eq 16

$$\log q_e = \log K_F + \frac{1}{n} \cdot \log C_e \tag{16}$$

where K_F (mg g^{-1}) is the Freundlich constant, which describes the adsorption capacity, and $1/n$ is the heterogeneity factor. It can be seen from Table 3 that the R^2 value for the Freundlich model was below 0.95, indicating that the experimental data deviated from the theoretical data; therefore, the Freundlich model was unsuitable.

Finally, to demonstrate the impact of our findings, we compiled and compared previously reported Cr(VI) adsorption properties of iron oxide, presented in Table 4. This demonstrated that iron oxides can be used for Cr(VI) adsorption but that their adsorption properties differ depending on their morphologies. As previously mentioned, the

Table 4. Iron Oxide Cr(VI) Adsorption Values from This Study and the Literature

iron oxide adsorbent material	pH	T (°C)	adsorption capacity (mg/g)	references
maghemite nanoparticles	2.5	25	19.2	49
3D hierarchical α-Fe$_2$O$_3$	3.0	25	34.4	50
α-Fe$_2$O$_3$ nanofibers	3.0	25	16.17	26
α-Fe$_2$O$_3$ nanoparticles	3.0	25	200	48
α-Fe$_2$O$_3$ nanofibers	6.0	25	90.9	55
Fe^{3+} oxide/hydroxide NP	4.0	25	31.5	51
flower-like α-Fe$_2$O$_3$	3.0	25	7.6	52
nanocrystalline iron oxide	2.0	25	2.29	53
α-Fe$_2$O$_3$ nanostructure	2.0	25	22.72	54
α-Fe$_2$O$_3$ nanowires	2.0	25	66.26	this study

adsorption capacity of Cr(VI) onto iron oxide is influenced by the pH of the solution, with a low pH being preferable to promote a higher adsorption capacity.[48] Another factor that affects Cr(VI) adsorption is the specific surface area that is available for adsorption. Nalbandian et al. achieved an improved adsorption capacity of 90.9 mg/g using small-diameter (i.e., higher surface area) α-Fe$_2$O$_3$ nanofibers.[55] The TEM and SEM images in Figures 2 and 4 allowed us to estimate the surface area provided by one NW to be approximately 204.28×10^{-15} m^2. On a 1 cm × 1 cm oxidized iron foil, we estimated there to be approximately 3×10^{10} NWs on the surface, assuming a homogeneous distribution; therefore, we consider our Cr(VI) adsorption capacity of 66.26 mg/g to be rather good. Although this is lower than the 90.9 mg/g values reported by Nalbandian et al.,[55] the use of α-Fe$_2$O$_3$ NWs on iron foils enables their simple removal from the target solution. This indicates that the formation of α-Fe$_2$O$_3$ NWs by the water vapor-assisted surface oxidation of iron has an excellent potential for the removal of harmful Cr(VI) from wastewater.

3. CONCLUSIONS

We investigated the high-temperature (700 and 800 °C) formation of iron oxide nanostructures through thermal oxidation in dry-air- and water vapor-assisted conditions. Oxidation at 700 °C led to the formation of coral-like nanostructures, whereas α-Fe$_2$O$_3$ NWs were obtained from oxidation at 800 °C. Water vapor-assisted thermal oxidation resulted in an increased rate of oxide formation and larger or denser coral-like or NW structures with high aspect ratios at 700 and 800 °C, respectively. Through systematically observing the oxidation process, we were able to describe the formation mechanism of the α-Fe$_2$O$_3$ NWs, which was a stress-driven mechanism through surface diffusion. Notably, NWs were produced after 5 min of oxidation, but the densest NWs with the highest aspect ratios were obtained only after 120 min. We then evaluated the Cr(VI) adsorption property of α-Fe$_2$O$_3$ NWs obtained from water vapor-assisted thermal oxidation at 800 °C for 2 h. A removal efficiency of 97% was achieved within 90 min using an aqueous Cr(VI) solution with a concentration of 225 mg/L. Finally, we investigated the adsorption equilibrium and kinetic models, which agreed with the Langmuir and pseudo-second-order kinetic models, respectively. The adsorption capacity of these α-Fe$_2$O$_3$ NWs was calculated to be 66.26 mg/g. This simple methodology for forming high-aspect-ratio α-Fe$_2$O$_3$ NWs through surface oxidation has a great potential for producing large-surface-area adsorbents to enable the simple removal of Cr ions from aqueous systems. The findings of this study will be beneficial and useful for the removal and mitigation of harmful Cr(VI) ions from wastewater.

4. EXPERIMENTAL PROCEDURES

The 1 × 1 cm iron foils (99.9%, Nilaco Corporation) were polished with a 2000 grit silicon carbide paper, ultrasonically cleaned in acetone, rinsed using deionized water, and then dried. Then, they were placed in an alumina crucible and positioned in the hot zone of a horizontal furnace. The furnace was progressively heated by 5 °C/min until the desired oxidation temperature was reached, which was either 700 or 800 °C. Once this temperature was reached, the furnace was purged with water vapor generated using a nebulizer (Omron

NE-C801). The evolution of the surface oxide was monitored using a field-emission electron microscope (FESEM) (Zeiss Supra 35 VP), and higher-magnification images were obtained using a high-resolution transmission electron microscope (HR-TEM) (Tecnai G^2 20 S-TWIN). Crystal structures were examined by taking X-ray diffraction (XRD) patterns (Bruker D8 Advance diffractometer) with a Cu Kα radiation source (λ = 0.154 nm) A Raman spectrometer (Renishaw RL633) was used for phase identification, and an X-ray photoelectron spectrophotometer (XPS) (Kratos Axis Ultra XPS Spectroscopy) with an Al X-ray radiation source was used for surface and elemental analysis.

To evaluate the Cr(VI) removal ability of the nanostructures, oxidized iron with α-Fe$_2$O$_3$ NWs was placed in Cr(VI) solutions of various concentrations between 225 and 300 mg/L, at room temperature. The pH of the solutions was adjusted to pH 2 by adding H$_2$SO$_4$ (27%). The assessment of the Cr(VI) content was performed using a diphenyl-carbazide (DPC) colorimetry method. DPC solution was prepared by diluting 0.25 g of 1,5-diphenylcarbazide in 50 mL of acetone, and a droplet was added into the Cr(VI) solutions. A color change in the solution to purple indicated the existence of Cr(VI). UV−visible (UV−vis) measurements were taken with a UV−vis spectrophotometer (PerkinElmer Lambda 35), and absorption values were recorded at a wavelength of 540 nm to detect Cr(VI).[37] The adsorption study was divided into two parts: equilibrium and kinetic. First, 50 mL solutions of Cr(VI) with concentrations ranging from 225 to 300 mg/L were prepared. The α-Fe$_2$O$_3$ NWs were then immersed in the Cr(VI) solution. During this adsorption process, bubbles, which were supplied by an air pump (Super X Classica) with an output of 250 L/h, were used for stirring the Cr(VI) solution. The amount of Cr(VI) adsorbed at the equilibrium condition (q_e) was calculated using eq 17

$$q_e = \frac{(C_o - C_e) \cdot V}{m} \tag{17}$$

where C_o and C_e are the initial and equilibrium concentrations of Cr(VI) (mg/L), respectively, V is the volume of solution used (L), and m is the mass of the adsorbent (g). For the kinetic study, the amount of Cr(VI) adsorbed at time t (q_t) was calculated using eq 18

$$q_t = \frac{(C_o - C_t) \cdot V}{m} \tag{18}$$

where C_t is the concentration of Cr(VI) at time t.

■ AUTHOR INFORMATION

Corresponding Authors

Wai Kian Tan − *Institute of Liberal Arts & Sciences, Toyohashi University of Technology, Toyohashi, Aichi 441-8580, Japan;* ⊙ orcid.org/0000-0002-0014-5475; Email: tan@las.tut.ac.jp

Zainovia Lockman − *Green Electronic Nanomaterials Group, School of Materials and Mineral Resources Engineering, Engineering Campus, Universiti Sains Malaysia, Nibong Tebal 14300 Penang, Malaysia;* ⊙ orcid.org/0000-0002-1535-8035; Email: zainovia@usm.my

Authors

Faisal Budiman − *Green Electronic Nanomaterials Group, School of Materials and Mineral Resources Engineering, Engineering Campus, Universiti Sains Malaysia, Nibong Tebal 14300 Penang, Malaysia; Department of Electrical Engineering, School of Electrical Engineering, Telkom University, Bandung 40257, Indonesia*

Go Kawamura − *Department of Electrical and Electronic Information Engineering, Toyohashi University of Technology, Toyohashi, Aichi 441-8580, Japan;* ⊙ orcid.org/0000-0001-6585-7636

Hiroyuki Muto − *Institute of Liberal Arts & Sciences and Department of Electrical and Electronic Information Engineering, Toyohashi University of Technology, Toyohashi, Aichi 441-8580, Japan*

Atsunori Matsuda − *Department of Electrical and Electronic Information Engineering, Toyohashi University of Technology, Toyohashi, Aichi 441-8580, Japan;* ⊙ orcid.org/0000-0002-6493-1205

Khairunisak Abdul Razak − *Green Electronic Nanomaterials Group, School of Materials and Mineral Resources Engineering, Engineering Campus, Universiti Sains Malaysia, Nibong Tebal 14300 Penang, Malaysia;* ⊙ orcid.org/0000-0003-0140-2418

Complete contact information is available at:
https://pubs.acs.org/10.1021/acsomega.1c04280

Notes

The authors declare no competing financial interest.

■ ACKNOWLEDGMENTS

■ REFERENCES

(1) Guertin, J.; Avakian, C. P; Jacobs, J. A. *Chromium (VI) handbook*; CRC Press: Florida, 2016.

(2) Rahman, Z.; Singh, V. P. The relative impact of toxic heavy metals (THMs)(arsenic (As), cadmium (Cd), chromium (Cr)(VI), mercury (Hg), and lead (Pb)) on the total environment: an overview. *Environ. Monit. Assess.* **2019**, *191*, 419.

(3) Lin, C.-H.; Lai, C.-H.; Peng, Y.-P.; Wu, P.-C.; Chuang, K.-Y.; Yen, T.-Y.; Xiang, Y.-K. Comparative health risk of inhaled exposure to organic solvents, toxic metals, and hexavalent chromium from the use of spray paints in Taiwan. *Environ. Sci. Pollut. Res.* **2019**, *26*, 33906−33916.

(4) Lejding, T.; Engfeldt, M.; Bruze, M.; Isaksson, M.; Svedman, C.; Zimerson, E.; Verma, K.; Mowitz, M. Skin application of glutathione and iron sulfate can inhibit elicitation of allergic contact dermatitis from hexavalent chromium. *Contact Dermatitis* **2019**, *82*, 45−53.

(5) Yu, J.-H.; Lu, J.-X.; Smollin, C.; Cheng, H.-T.; Seak, C.-J.; Chen, H.-Y. N-acetylcysteine and ascorbic acid therapy for acute hepatic injury after hexavalent chromium ingestion. *J. Clin. Pharm. Ther.* **2020**, *45*, 208−210.

(6) Rosli, S.-A.; Alias, N.; Bashirom, N.; Ismail, S.; Tan, W.-K.; Kawamura, G.; Matsuda, A.; Lockman, Z. Hexavalent Chromium Removal via Photoreduction by Sunlight on Titanium−Dioxide Nanotubes Formed by Anodization with a Fluorinated Glycerol−Water Electrolyte. *Catalysts* **2021**, *11*, 376.

(7) WHO *Guidelines for drinking-water quality*; World Health Organization: Geneva, 2011.

(8) Gao, Z.; Yang, H.; Fu, X.; Jin, Q.; Wu, Q.; Kang, L.; Wu, J. Efficient photoreduction of Cr (VI) on TiO_2/functionalized activated carbon (TiO_2/AC-AEMP): improved adsorption of Cr (VI) and induced transfer of electrons. *Environ. Sci. Pollut. Res.* **2020**, *27*, 17446−17457.

(9) Bashirom, N.; Tan, W.-K.; Kawamura, G.; Matsuda, A.; Lockman, Z. Comparison of ZrO_2, TiO_2, and α-Fe_2O_3 nanotube arrays on Cr (VI) photoreduction fabricated by anodization of Zr, Ti, and Fe foils. *Mater. Res. Express* **2020**, *7*, No. 055013.

(10) Hu, B.; Ai, Y.; Jin, J.; Hayat, T.; Alsaedi, A.; Zhuang, L.; Wang, X. Efficient elimination of organic and inorganic pollutants by biochar and biochar-based materials. *Biochar* **2020**, *2*, 47−64.

(11) Xie, B.; Shan, C.; Xu, Z.; Li, X.; Zhang, X.; Chen, J.; Pan, B. One-step removal of Cr (VI) at alkaline pH by UV/sulfite process: reduction to Cr (III) and in situ Cr (III) precipitation. *Chem. Eng. J.* **2017**, *308*, 791−797.

(12) Zheng, Y.; Yan, Y.; Yu, L.; Li, H.; Jiao, B.; Shiau, Y.; Li, D. Synergism of citric acid and zero-valent iron on Cr (VI) removal from real contaminated soil by electrokinetic remediation. *Environ. Sci. Pollut. Res.* **2020**, *27*, 5572−5583.

(13) Abdullah, N.; Yusof, N.; Shah, M. H. A.; Ikhsan, S.-N.-W.; Ng, Z.-C.; Maji, S.; Lau, W.-J.; Jaafar, J.; Ismail, A.-F.; Ariga, K. Hydrous ferric oxide nanoparticles hosted porous polyethersulfone adsorptive membrane: chromium (VI) adsorptive studies and its applicability for water/wastewater treatment. *Environ. Sci. Pollut. Res.* **2019**, *26*, 20386−20399.

(14) Hu, B.; Wang, H.; Liu, R.; Qiu, M. Highly efficient U (VI) capture by amidoxime/carbon nitride composites: Evidence of EXAFS and modeling. *Chemosphere* **2021**, *274*, 129743.

(15) Zhang, R.; Zeng, Q.; Guo, P.; Cui, Y.; Sun, Y. Efficient capture of Cr (VI) by carbon hollow fibers with window-like structure. *Environ. Sci. Pollut. Res.* **2020**, *27*, 16763−16773.

(16) Liu, X.; Pang, H.; Liu, X.; Li, Q.; Zhang, N.; Mao, L.; Qiu, M.; Hu, B.; Yang, H.; Wang, X. Orderly porous covalent organic frameworks-based materials: superior adsorbents for pollutants removal from aqueous solutions. *Innovation* **2021**, *2*, 100076.

(17) Liang, L.; Xi, F.; Tan, W.; Meng, X.; Hu, B.; Wang, X. Review of organic and inorganic pollutants removal by biochar and biochar-based composites. *Biochar* **2021**, *3*, 255−281.

(18) Rasheed, A.; Carvalho, A.-A.-C.; de Carvalho, G.-G.-A.; Ghous, T.; Nomura, C.-S.; Esposito, B.-P. Chromium removal from aqueous solutions using new silica gel conjugates of desferrioxamine or diethylenetriaminepentaacetic acid. *Environ. Sci. Pollut. Res.* **2020**, *27*, 1−10.

(19) Cornell, R. M; Schwertmann, U. *The iron oxides: structure, properties, reactions, occurrences and uses*; John Wiley & Sons: New Jersey, 2003.

(20) Bahmani, P.; Maleki, A.; Daraei, H.; Rezaee, R.; Khamforoush, M.; Athar, S.-D.; Gharibi, F.; Ziaee, A.-H.; McKay, G. Application of modified electrospun nanofiber membranes with α-Fe_2O_3 nanoparticles in arsenate removal from aqueous media. *Environ. Sci. Pollut. Res.* **2019**, *26*, 21993−22009.

(21) Chiavola, A.; D'Amato, E.; Boni, M. R. Comparison of different iron oxide adsorbents for combined arsenic, vanadium, and fluoride removal from drinking water. *Int. J. Environ. Sci. Technol.* **2019**, *16*, 6053−6064.

(22) Fayazi, M.; Afzali, D.; Ghanei-Motlagh, R.; Iraji, A. Synthesis of novel sepiolite−iron oxide−manganese dioxide nanocomposite and application for lead (II) removal from aqueous solutions. *Environ. Sci. Pollut. Res.* **2019**, *26*, 18893−18903.

(23) Sruthi, P.-D.; Sahithya, C.-S.; Justin, C.; SaiPriya, C.; Bhavya, K.-S.; Senthilkumar, P.; Samrot, A. V. Utilization of Chemically Synthesized Super Paramagnetic Iron Oxide Nanoparticles in Drug Delivery, Imaging and Heavy Metal Removal. *J. Cluster Sci.* **2019**, *30*, 11−24.

(24) Khan, F.-S.-A.; Mubarak, N.-M.; Khalid, M.; Walvekar, R.; Abdullah, E.-C.; Mazari, S.-A.; Nizamuddin, S.; Karri, R.-R. Magnetic nanoadsorbents' potential route for heavy metals removal—a review. *Environ. Sci. Pollut. Res.* **2020**, *27*, 24342−24356.

(25) Singaraj, S.-G.; Mahanty, B.; Balachandran, D.; Padmaprabha, A. Adsorption and desorption of chromium with humic acid coated iron oxide nanoparticles. *Environ. Sci. Pollut. Res.* **2019**, *26*, 30044−30054.

(26) Ren, T.; He, P.; Niu, W.; Wu, Y.; Ai, L.; Gou, X. Synthesis of α-Fe_2O_3 nanofibers for applications in removal and recovery of Cr (VI) from wastewater. *Environ. Sci. Pollut. Res.* **2013**, *20*, 155−162.

(27) Tan, W.-K.; Razak, K.-A.; Ibrahim, K.; Lockman, Z. Oxidation of etched Zn foil for the formation of ZnO nanostructure. *J. Alloys Compd.* **2011**, *509*, 6806−6811.

(28) Deng, J.; Liu, J.; Dai, H.; Wang, W. Preparation of α-Fe_2O_3 nanowires through electrospinning and their Ag_3PO_4 heterojunction composites with enhanced visible light photocatalytic activity. *Ferroelectrics* **2018**, *528*, 58−65.

(29) Ponti, A.; Raza, M.-H.; Pantò, F.; Ferretti, A.-M.; Triolo, C.; Patanè, S.; Pinna, N.; Santangelo, S. Structure, Defects, and Magnetism of Electrospun Hematite Nanofibers Silica-Coated by Atomic Layer Deposition. *Langmuir* **2020**, *36*, 1305−1319.

(30) Sun, X.; Sun, X.; Liu, X.; Liu, R.; Li, S.; Shen, M.; Li, Q. One-dimensional Mg^{2+}-induced α-Fe_2O_3 nanowires for high-performance supercapacitor. *Results Mater.* **2020**, *5*, 100052.

(31) Azeez, N. A.; Dash, S. S.; Gummadi, S.-N.; Deepa, V. S. Nano-remediation of toxic heavy metal contamination: Hexavalent chromium [Cr (VI)]. *Chemosphere* **2021**, *266*, 129204.

(32) Rahmat, S.-T.; Chin, O. Y.; Tan, W. K.; Kawamura, G.; Matsuda, A.; Lockman, Z. Hierarchical Porous α-Fe_2O_3 Formation by Thermal Oxidation of Iron as Catalyst for Cr (VI) Reduction. *J. Phys.: Conf. Ser.* **2018**, *1082*, No. 012044.

(33) Rahmat, S.-T.; Hong, C.-Y.; Budiman, F.; Tan, W.-K.; Kawamura, G.; Matsuda, A.; Lockman, Z. Tailoring Parameters to Produce Nanowires on Metal Surface via Surface Oxidation Process. *J. Phys.: Conf. Ser.* **2018**, *1082*, No. 012052.

(34) Srivastava, H.; Srivastava, A.-K.; Babu, M.; Rai, S.; Ganguli, T. Topotaxial growth of α-Fe_2O_3 nanowires on iron substrate in thermal annealing method. *J. Appl. Phys.* **2016**, *119*, 244311.

(35) Budiman, F.; Bashirom, N.; Tan, W.-K.; Razak, K.-A.; Matsuda, A.; Lockman, Z. Rapid nanosheets and nanowires formation by thermal oxidation of iron in water vapour and their applications as Cr (VI) adsorbent. *Appl. Surf. Sci.* **2016**, *380*, 172−177.

(36) Rahmat, S.-T.; Tan, W.-K.; Kawamura, G.; Matsuda, A.; Lockman, Z. Synthesis of rutile TiO_2 nanowires by thermal oxidation of titanium in the presence of KOH and their ability to photoreduce Cr (VI) ions. *J. Alloys Compd.* **2020**, *812*, 152094.

(37) Onchoke, K.-K.; Sasu, S.-A. Determination of Hexavalent Chromium (Cr (VI)) concentrations via ion chromatography and UV-Vis spectrophotometry in samples collected from nacogdoches wastewater treatment plant, East Texas (USA). *Adv. Environ. Chem.* **2016**, *2016*, 152094.

(38) Yuan, L.; Wang, Y.; Cai, R.; Jiang, Q.; Wang, J.; Li, B.; Sharma, A.; Zhou, G. The origin of hematite nanowire growth during the thermal oxidation of iron. *Mater. Sci. Eng., B* **2012**, *177*, 327−336.

(39) Taniguchi, K.; Kitazawa, N. Characterization of α-Fe_2O_3 nanorod arrays prepared by a quasi-topotactic transformation of β-FeOOH nanowire-like arrays. *J. Phys. Chem. Solids* **2020**, *147*, 109632.

(40) Ma, H.; Hwang, J.-B.; Chae, W.-S.; Chung, H.-S.; Choi, S.-H.; Mahadik, M.-A.; Lee, H.-H.; Jang, J.-S. Magnetron sputtering strategy for Zr-Fe_2O_3 nanorod photoanode fabricated from ZrO_x/β-FeOOH nanorods for photoelectrochemical water splitting. *Appl. Surf. Sci.* **2021**, *549*, 149233.

(41) Khanna, A. S. *Introduction to high temperature oxidation and corrosion*; ASM international: Delhi, 2002.

(42) Fujii, C.-T.; Meussner, R.-A. The Mechanism of the High-Temperature Oxidation of Iron-Chromium Alloys in Water Vapor. *J. Electrochem. Soc.* **1964**, *111*, 1215.

(43) Lange, N. A. *Lange's Handbook of Chemistry*; McGraw-Hill: New York, 1985.

(44) Zhu, Y.; He, X.; Xu, J.; Fu, Z.; Wu, S.; Ni, J.; Hu, B. Insight into efficient removal of Cr (VI) by magnetite immobilized with

Lysinibacillus sp. JLT12: Mechanism and performance. *Chemosphere* **2021**, *262*, 127901.

(45) Roy, A.; Velusamy, S.; Mallick, T. K.; Sundaram, S. Synergistic effect of nanoflower-like CdS for removal of highly toxic aqueous Cr (VI). *Mater. Lett.* **2020**, *270*, 127734.

(46) Alias, N.; Hussain, Z.; Tan, W. K.; Kawamura, G.; Muto, H.; Matsuda, A.; Lockman, Z. Nanoporous anodic Nb_2O_5 with pore-in-pore structure formation and its application for the photoreduction of Cr(VI). *Chemosphere* **2021**, *283*, 131231.

(47) Aredes, S.; Klein, B.; Pawlik, M. The removal of arsenic from water using natural iron oxide minerals. *J. Cleaner Prod.* **2013**, *60*, 71−76.

(48) Adegoke, H.-I.; AmooAdekola, F.; Fatoki, O.-S.; Ximba, B.-J. Adsorption of Cr (VI) on synthetic hematite (α-Fe_2O_3) nanoparticles of different morphologies. *Korean J. Chem. Eng.* **2014**, *31*, 142−154.

(49) Hu, J.; Chen, G.; Lo, I.-M. C. Removal and recovery of Cr (VI) from wastewater by maghemite nanoparticles. *Water Res.* **2005**, *39*, 4528−4536.

(50) Liu, Z.; Yu, R.; Dong, Y.; Li, W.; Lv, B. The adsorption behavior and mechanism of Cr(VI) on 3D hierarchical α-Fe_2O_3 structures exposed by (001) and non-(001) planes. *Chem. Eng. J.* **2017**, *309*, 815−823.

(51) Zelmanov, G.; Semiat, R. Iron (Fe^{+3}) oxide/hydroxide nanoparticles-based agglomerates suspension as adsorbent for chromium (Cr^{+6}) removal from water and recovery. *Sep. Purif. Technol.* **2011**, *80*, 330−337.

(52) Cao, C.-Y.; Qu, J.; Yan, W.-S.; Zhu, J.-F.; Wu, Z.-Y.; Song, W.-G. Low-cost synthesis of flowerlike α-Fe_2O_3 nanostructures for heavy metal ion removal: adsorption property and mechanism. *Langmuir* **2012**, *28*, 4573−4579.

(53) Gusain, D.; Srivastava, V.; Sillanpää, M.; Sharma, Y.-C. Kinetics and isotherm study on adsorption of chromium on nano crystalline iron oxide/hydroxide: linear and nonlinear analysis of isotherm and kinetic parameters. *Res. Chem. Intermed.* **2016**, *42*, 7133−7151.

(54) Jia, Z.; Wang, Q.; Ren, D.; Zhu, R. Fabrication of one-dimensional mesoporous α-Fe_2O_3 nanostructure via self-sacrificial template and its enhanced Cr (VI) adsorption capacity. *Appl. Surf. Sci.* **2013**, *264*, 255−260.

(55) Nalbandian, M.-J.; Zhang, M.; Sanchez, J.; Choa, Y.-H.; Nam, J.; Cwiertny, D.-M.; Myung, N.-V. Synthesis and optimization of Fe_2O_3 nanofibers for chromate adsorption from contaminated water sources. *Chemosphere* **2016**, *144*, 975−981.

(56) Zhou, N.; Gong, K.; Hu, Q.; Cheng, X.; Zhou, J.; Dong, M.; Wang, N.; Ding, T.; Qiu, B.; Guo, Z. Optimizing nanocarbon shell in zero-valent iron nanoparticles for improved electron utilization in Cr (VI) reduction. *Chemosphere* **2020**, *242*, 125235.

(57) Richard, F. C.; Bourg, A. C. M. Aqueous geochemistry of chromium: a review. *Water Res.* **1991**, *25*, 807−816.

(58) Largitte, L.; Pasquier, R. A review of the kinetics adsorption models and their application to the adsorption of lead by an activated carbon. *Chem. Eng. Res. Des.* **2016**, *109*, 495−504.

(59) Foo, K.-Y.; Hameed, B.-H. Insights into the modeling of adsorption isotherm systems. *Chem. Eng. J.* **2010**, *156*, 2−10.